RESEARCH ARTICLE

Check for updates

A bimetallic CoZn metal–organic-framework derived CoZnS@NSC Co-catalyst loaded on g-C₃N₄ for significantly augmented photocatalytic H₂ evolution†

Xiao-Jie Lu,‡[a] Ikram Ullah,‡[a] Jing-Han Li,[a] Shuai Chen,[a] Cheng-Zong Yuan [ID] [b] and An-Wu Xu [ID] *[a]

The main existing issues in graphitic carbon nitride (g-C₃N₄) based photocatalytic hydrogen (H₂) production include poor separation and transfer of photogenerated charge carriers and low optical absorption. Thus, the construction of a multicomponent co-catalyst and its integration with g-C₃N₄ to facilitate the transport and separation of photoexcited charge carriers are regarded as a promising approach for augmenting the photocatalytic H₂ production activity. In this study, we report CoZnS@NSC-*X*/g-C₃N₄ (where *X* indicates sulfidation times of 15, 30, 45, and 60 min) nanocomposites constructed from a CoZn-MOF derived CoS₂, Co₃S₄ and ZnS intercalated nitrogen/sulfur-doped carbon (CoZnS@NSC) nanoparticle co-catalyst and g-C₃N₄ for H₂ production from water splitting. The maximum photocatalytic H₂ evolution rate (610.8 μmol h⁻¹ g⁻¹) of the CoZnS@NSC-15/g-C₃N₄ heterostructure, with an optimized CoZnS@NSC loading of 10 wt% and 15 min sulfidation, is nearly 3.7 and 290.9 times higher than those of unsulfidated CoZn@NC/g-C₃N₄ and bare g-C₃N₄, respectively. This significantly boosted photocatalytic performance is attributed to the efficient separation and transfer of electron–hole (e⁻/h⁺) pairs and electronic conductivity caused by the appropriate sulfidation time and loading amount of CoZnS@NSC nanoparticles. This work offers a facile approach to designing metal–organic framework derived co-catalyst modified semiconductor-based photocatalysts for high-performance in practical applications.

1. Introduction

The growing need for energy and the rising environmental crisis have led to substantial attention toward the exploration of sustainable energy sources.[1,2] At present, H₂ energy is considered as the cleanest fuel since its only combustion byproduct is water.[3] The promising strategy of visible-light driven

[a] Division of Nanomaterials and Chemistry, Hefei National Research Center for Physical Sciences at the Microscale, University of Science and Technology of China, Hefei, Anhui 230026, P. R. China. E-mail: anwuxu@ustc.edu.cn

[b] School of Rare Earths, University of Science and Technology of China, Hefei, Anhui 230026, P. R. China

†Electronic supplementary information (ESI) available: Additional experimental and characterization results of TGA, Raman spectrum, EDX analysis, N₂ adsorption–desorption isotherms, pore size distribution, Tauc plots, VB XPS, and UPS. Photocatalytic H₂ evolution rate of CoZnS@NSC-15/g-C₃N₄ under various CoZnS@NSC-15 loading amounts. XRD and XPS spectra of CoZnS@NSC-15/g-C₃N₄ before and after the cycle test. Photocatalytic equipment image of our water splitting system. Comparison table of physicochemical properties and kinetic analysis of the emission decay of the as-prepared samples. Comparison table of our study's photocatalytic H₂ evolution rate with previous reports. See DOI: https://doi.org/10.1039/d4qi00644e

‡These authors contributed equally to this work.

photocatalytic H₂ production from water splitting, which utilizes abundant solar energy has attracted considerable attention.[4,5] Various semiconductors, including TiO₂, CdS, ZnO, and g-C₃N₄ have been employed to achieve photocatalytic H₂ production.[6–8] Nevertheless, there are still many challenges in the practical applications of these semiconductors that need to be addressed, such as the development of cost-effective and efficient photocatalysts with enhanced e⁻/h⁺ separation efficiency.[9] Among these, g-C₃N₄ has attracted significant attention due to its suitable energy band position, good chemical stability, cost-effectiveness, and simple preparation process.[10,11] However, the poor optical absorption and rapid recombination of photogenerated e⁻/h⁺ pairs of g-C₃N₄ hinder its photocatalytic activity. Therefore, various modification strategies have been employed to improve the visible-light response and photogenerated e⁻/h⁺ separation efficiency of g-C₃N₄, such as doping with heteroatoms,[12,13] modulation of morphology,[14,15] construction of heterojunctions,[16–18] and loading of co-catalysts.[19,20] Meanwhile, due to the difficulties of separating photogenerated e⁻/h⁺ pairs and the strong driving force of redox reactions, g-C₃N₄ continues to rely on noble metal co-catalysts and sacrificial agents to achieve

This journal is © the Partner Organisations 2024

Inorg. Chem. Front., 2024, **11**, 3435–3445 | **3435**

efficient photocatalytic H_2 production from water splitting.[21–23] Recently, in most photocatalytic H_2 production processes, the noble metal Pt served as a co-catalyst. The incorporation of noble metal nanoparticles onto the g-C_3N_4 surface effectively reduced the overpotential in H_2 evolution, thereby promoting the photocatalytic H_2 generation efficiency from water. Nevertheless, the shortage and high cost of noble metals have seriously hindered their large-scale applications in photocatalytic H_2 evolution. Consequently, economical non-noble metal co-catalysts, such as MoS_2, NiS, Cu_3P, and CoP,[24–27] have been employed as alternatives to noble metals, thus promoting the photocatalytic performance.

Indeed, co-catalysts play a key role in augmenting the photocatalytic performance of photocatalysts. It has been found that multi-component co-catalysts exhibit higher photocatalytic activity and charge transfer efficiency compared to single-component co-catalysts. Peng et al.[28] synthesized NiCoP-fabricated g-C_3N_4, which demonstrated elevated photocatalytic activity compared to Ni_2P and CoP-fabricated g-C_3N_4. Specifically, Co-based composites (CoP, CoS_2, Co_3S_4 etc.) have gained extensive research attention owing to their promising photocatalytic performance and environment-friendly characteristics. Ji et al.[29] reported ZIF-67 derived N,P-doped composites of C-incorporated CoP/Co nanoparticles to boost the photocatalytic performance of g-C_3N_4. The Munichandraiah[30] group reported that the prepared Ni–Co–S electrocatalysts significantly boost H_2 generation. Typically, the construction of bimetallic sulfides by integrating transition metal elements such as Mn, Fe, Co, Ni, and Zn achieved boosted photocatalytic performance.[31] Based on their electronic configuration, transition metal species have a large number of unpaired d-orbital electrons, which can readily promote the chemisorption of H_2, making it possible to catalyze the H_2 generation.[32] Nowadays, bimetallic sulfides are being extensively employed as catalysts for electrocatalytic H_2 evolution reaction, while relatively less research has been reported for photocatalytic H_2 production. Furthermore, in the construction of bimetallic sulfide/g-C_3N_4 composite photocatalysts, the poor contact at the interface during the reaction process results in severe aggregation of bimetallic sulfide, thus influencing the catalytic activity. Therefore, it is essential to hybridize bimetallic sulfides with carbonaceous materials via an efficient approach to address this challenge.[33]

Recently, metal–organic-framework (MOF) materials have emerged as a class of crystalline organic–inorganic hybrid materials composed of metal ions and organic ligands, and are widely used in many fields due to their special metallic framework structure.[34–37] However, MOF materials are rarely applied directly to H_2 production from water splitting because of their poor intrinsic electrical conductivity and stability, as well as the fact that the reactive metal center can be blocked by organic ligands.[38,39] MOF materials formed by the coordination of transition metals with organic ligands have been widely used as templates or precursors for the synthesis of transition metal@porous carbon-based composites by thermal decomposition of the carbonized original skeleton.[40,41] The derivatives of the MOF materials including oxides,[42] sulfides,[43,44] and phosphides[45,46] can be well dispersed in a porous carbon substrate. Generally, the inherent hierarchical pore structure and large specific surface area of the MOF precursor can expose more catalytic sites. Carbon-based materials serve as efficient co-catalysts with g-C_3N_4, capturing electrons quickly and accelerating the separation of photogenerated charges, besides serving as an intermediate bridge in the photocatalytic water splitting over g-C_3N_4,[47–49] resulting in high photocatalytic activity. Therefore, decorating g-C_3N_4 with a porous polyhedral co-catalyst with several active layers could be more effective at boosting its photocatalytic performance.

Zeolite imidazolium framework (ZIF) materials are zeolite-like three-dimensional topological MOF materials with high metal ion content and abundant carbon and nitrogen ligands. These features make them excellent precursor templates for constructing metal@porous carbon-based composites.[50,51] However, ZIF-67 and ZIF-8 possess similar crystal structures with transition metals Co and Zn as central ions. This resemblance allows the preparation of Co/Zn bimetallic MOF materials, which can be used as precursors for the synthesis of bimetallic sulfides. Herein, a nanocomposite of nitrogen/sulfur-doped carbon-encapsulated CoS_2, Co_3S_4, and ZnS nanoparticles was derived from ZIF-67 and ZIF-8 via an annealing–sulfurization strategy (CoZnS@NSC). Then the obtained CoZnS@NSC nanoparticles were used as a multicomponent co-catalyst for g-C_3N_4 to promote its photocatalytic hydrogen production performance. A series of CoZnS@NSC-X/g-C_3N_4 (X indicates the sulfidation times of 10, 15, 30, and 60 min) photocatalysts were designed, and they show enhanced photocatalytic H_2 generation activity from water splitting under visible-light ($\lambda \geq$ 400 nm) compared to bare g-C_3N_4. The optimal CoZnS@NSC-15/g-C_3N_4 exhibits the highest photocatalytic H_2 evolution rate (610.8 μmol h^{-1} g^{-1}), which is 290.9 and 3.7 times higher than those of bare g-C_3N_4 and unsulfidated CoZn@NC/g-C_3N_4 samples. This significantly steered photocatalytic activity is associated with the synergistic effect generated by the firm interaction of CoS_2, Co_3S_4, and ZnS nanoparticles with the carbon substrate and its integration with g-C_3N_4.

2. Experimental section

2.1 Synthesis of pure g-C_3N_4

In a typical synthesis procedure, 10 g of urea was introduced into an alumina crucible. The crucible was then placed in a muffle furnace and subjected to calcination under an air atmosphere at 550 °C for 4 hours with a ramp rate of 5 °C min^{-1}. Afterward, the material was cooled naturally to ambient temperature, resulting in a pale-yellow product.

2.2 Preparation of the CoZn-MOF

Firstly, $Co(NO_3)_2\cdot6H_2O$ (291 mg) and $Zn(NO_3)_2\cdot6H_2O$ (149 mg) were mixed in 35 mL of methanol and thoroughly stirred. Then, 2-methylimidazole (492 mg) was dissolved in 35 mL of

3436 | Inorg. Chem. Front., 2024, **11**, 3435–3445

This journal is © the Partner Organisations 2024

methanol to form a transparent solution and quickly transferred to the first solution followed by stirring for 30 minutes and maintained at room temperature for 24 hours. Afterward, the mixed solution was centrifuged at 10 000 RPM, resulting in a white precipitate, followed by washing with methanol several times and the purple powder was dried in a vacuum oven at 40 °C overnight to obtain the CoZn-MOF.

2.3 Synthesis of CoZn@NC

The obtained CoZn-MOF powder was taken in a porcelain boat and then placed in the tube furnace followed by heating at 350 °C for 1.5 h with a ramp rate of 10 °C min^{-1} under a 5% H$_2$/95%Ar atmosphere. Subsequently, it was naturally cooled to room temperature and then recalcined at 550 °C for 3.5 h. The resulting carbonized CoZn-MOF samples were obtained and indicated as CoZn@NC.

2.4 Synthesis of CoZnS@NSC

The CoZnS@NSC sample was synthesized by the sulfidation reaction of CoZn@NC with L-cysteine. The method involved pouring CoZn@NC and L-cysteine in a mass ratio of 1 : 5 into two porcelain boats, and then placing them side by side in the middle of a tube furnace, which was heated to 350 °C for 15, 30, 45, and 60 min under an Ar atmosphere at a ramp rate of 10 °C min^{-1}. Finally, it was cooled down to room temperature, and the resulting composite was named CoZnS@NSC-X, where X (X = 15, 30, 45, and 60 min) represents the duration of the sulfidation reaction.

2.5 Synthesis of CoZnS@NSC/g-C$_3$N$_4$

The resultant CoZnS@NSC (20 mg) and g-C$_3$N$_4$ (180 mg) were mixed in a mortar containing 1 mL of ethanol and then vigorously ground for 1 h until the ethanol solution evaporated to produce a powder followed by drying in a vacuum oven at 40 °C for 2 h. The obtained samples were labeled as CoZnS@NSC-X/g-C$_3$N$_4$, where X is the sulfide reaction time. The counterpart CoZn@NC/g-C$_3$N$_4$ was obtained by grinding the same mass ratio of CoZn@NC and g-C$_3$N$_4$.

3. Results and discussion

According to our design scheme, composite co-catalysts of nitrogen/sulfur-doped carbon wrapped CoS$_2$, Co$_3$S$_4$, and ZnS nanoparticles derived from ZIF-67 and ZIF-8 with the addition of L-cysteine were prepared *via* the simple annealing–sulfurization strategy and used to modify g-C$_3$N$_4$ to form nanocomposite photocatalysts, and the preparation process is illustrated in Fig. 1a (see details in the Experimental section). Firstly, the successful assembly of the CoZn-MoF was obtained using Co(NO$_3$)$_2$·6H$_2$O, Zn(NO$_3$)$_2$·6H$_2$O, and 2-methylimidazole in methanol according to a previous report.[52] Secondly, the CoZn-MOF precursor was subjected to annealing to achieve the carbonized CoZn@NC nanoparticles. Then, CoZnS@NSC-X (where X = 15, 30, 45, and 60 min, which indicate the sulfidation times) was achieved *via* a simple sulfidation of CoZn@NC.
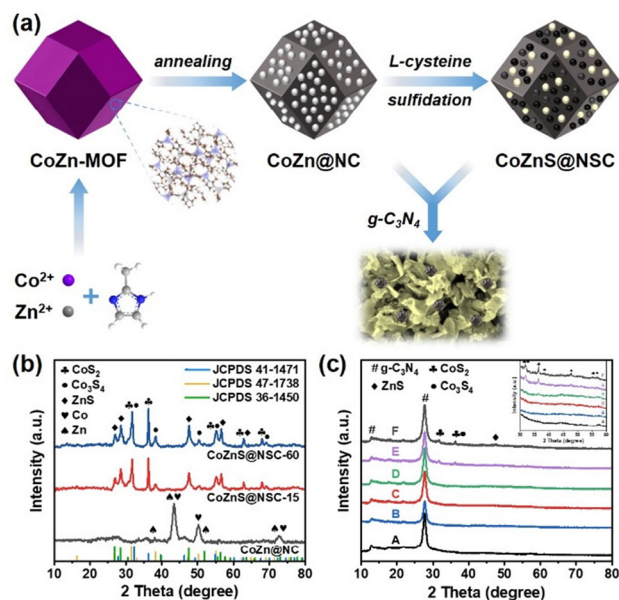

Fig. 1 (a) Schematic diagram of the synthesis of CoZn-MOF, CoZn@NC, CoZn@NC/g-C$_3$N$_4$, CoZnS@NSC, and CoZnS@NSC-X/g-C$_3$N$_4$ samples. XRD patterns of (b) CoZn@NC, CoZnS@NSC-15, and CoZnS@NSC-60 nanoparticles and (c) g-C$_3$N$_4$ (A), CoZn@NC/g-C$_3$N$_4$ (B), and CoZnS@NSC/g-C$_3$N$_4$ after sulfidation for 15 (C), 30 (D), 45 (E), and 60 min (F).

Finally, CoZnS@NSC-X/g-C$_3$N$_4$ was obtained through mixing of CoZnS@NSC-X with a specific amount of g-C$_3$N$_4$ in a mortar followed by drying in a microwave oven. As depicted in Fig. S1,† thermogravimetric analysis (TGA) tests reveal that the designed CoZn@NC/g-C$_3$N$_4$ and CoZnS@NSC-15/g-C$_3$N$_4$ nanoheterostructures exhibit robust and high stability around 500 °C, which is relatively similar to that of bare g-C$_3$N$_4$.

The phase purity and crystal structure of the as-synthesized samples were determined using X-ray diffraction (XRD). As presented in Fig. 1b, the sharp peaks of Co and Zn can be seen in CoZn@NC (Co: JCPDS 15-0806, Zn: JCPDS 04-0831). For the sulfidated CoZnS@NSC-15 and CoZnS@NSC-60 samples, the sharp diffraction peaks of CoS$_2$, Co$_3$S$_4$, and ZnS can be clearly observed, which are in alignment with the characteristic peaks of the standard cards for CoS$_2$ (JCPDS: 41-1471), Co$_3$S$_4$ (JCPDS: 47-1738), and ZnS (JCPDS: 36-1450). However, no diffraction peaks of metallic Co and Zn nanoparticles are observed, suggesting that Co and Zn were completely converted to sulfides after sulfidation treatment. Fig. 1c shows the XRD patterns of pristine g-C$_3$N$_4$, CoZn@NC/g-C$_3$N$_4$, and CoZnS@NSC-X/g-C$_3$N$_4$ photocatalysts. For bare g-C$_3$N$_4$, two distinctive diffraction peaks are detected at 12.8° (100) and 27.7° (002), corresponding to the in-plane structural packing of tri-*s*-triazine units and internal-layer packing of carbon nitride, respectively.[53] The XRD patterns of CoZnS@NSC-X/g-C$_3$N$_4$ samples reveal the existence of both characteristic peaks associated with pristine g-C$_3$N$_4$. In addition, the diffraction peaks for CoS$_2$, Co$_3$S$_4$, and ZnS can be clearly observed with the increase

This journal is © the Partner Organisations 2024

Inorg. Chem. Front., 2024, **11**, 3435–3445 | **3437**

in the sulfidation time. This result indicates the successful loading of CoZnS@NSC onto g-C_3N_4.

Furthermore, the structures of CoZn@NC and CoZnS@NSC-15 were further analyzed using Raman spectroscopy (Fig. S2†). For both CoZn@NC and CoZnS@NSC-15 samples, the presence of nitrogen/sulfur co-doped carbon (NSC) is confirmed by the identification of two peaks at 1330 and 1575 cm^{-1}, which correspond to the D and G bands, respectively.[29,54] Moreover, the ratio of the peak intensity of the D and G bands (I_D/I_G) can serve as a metric for measuring the degree of disorder in carbon materials.[55–57] The measured I_D/I_G value for CoZnS@NSC-15 is 0.95, which is slightly higher than that of unsulfidated CoZn@NC (0.91). This increment is associated with the sulfidation treatment of CoZn@NC, resulting in a rise in carbon defects and disorder in the nanoparticles, which obviously promote the electronic properties of the nanocomposites.

The morphologies of the as-obtained samples were examined using scanning electron microscopy (SEM), transmission electron microscopy (TEM), high-resolution transmission electron microscopy (HRTEM), high-angle annular dark-field scanning transmission electron microscopy (HAADF-STEM) and energy dispersive X-ray spectroscopy (EDX). The SEM image (Fig. 2a) shows the successful synthesis of CoZn-MoF nanoparticles, indicating a uniform and consistent polyhedral morphology. The SEM image of the synthesized CoZn@NC illustrates a rough surface embedded by the constructed nitrogen-doped carbon (NC); in addition it shows a smaller diameter than the CoZn-MOF caused by the shrinkage of the material during the carbonization process (Fig. 2b), indicating that the carbonization treatment changed the ideal morphology of the CoZn-MoF precursor. As seen in Fig. 2c, the SEM image of sulfidated CoZnS@NSC-15 nanoparticles shows an irregular morphology, indicating that sulfidation treatment further altered the textural properties of the CoZn-MoF precursor. The SEM image of the CoZnS@NSC-15/g-C_3N_4 nanocomposite shows a typical layered nanosheet-like structure, although CoZnS@NSC-15 nanoparticles were no longer visible (Fig. 2d).

The TEM images of CoZn-MOF, CoZn@NC, and CoZnS@NSC-15 samples are demonstrated in Fig. 2e–g, which are consistent with the SEM results. However, the TEM image of CoZnS@NSC-15/g-C_3N_4 clearly showed the presence of CoZnS@NSC-15 nanoparticles (Fig. 2h). As depicted in Fig. 2i, the HRTEM image of CoZnS@NSC-15/g-C_3N_4 clearly demonstrates that ZnS, Co_3S_4, and CoS_2 nanoparticles are uniformly distributed in the g-C_3N_4 framework. Moreover, the different lattice spacings observed from the figure correspond to the (110) and (002) crystal planes of ZnS, the (200) and (210) crystal planes of CoS_2, and the (400) crystal plane of Co_3S_4, respectively. Furthermore, HAADF-STEM images and their corresponding EDX elemental mapping images obviously show the uniform distribution of C, N, S, Co, and Zn elements in the CoZnS@NSC-15/g-C_3N_4 nanocomposite (Fig. 2j). As shown in Fig. S3,† EDX spectral analysis shows that the atomic ratio of Zn and Co in the product is about 1 : 2, which is in agreement with our feeding ratio. Taken together, the morphological results confirm the successful synthesis of CoZnS@NSC-15/g-C_3N_4.

The specific surface area, pore size distribution, and pore volume of the as-prepared samples were tested using N_2 adsorption–desorption isotherms. As shown in Fig. S4,† all samples exhibit type IV sorption isotherms with H3 hysteresis loops, indicating the presence of mesopores in the material.[58,59] According to the Brunauer–Emmett–Teller (BET) calculation method and the BJH pore size distribution, the specific surface area, pore volume, and pore size distribution of the as-prepared material were calculated.[60] The as-synthesized CoZnS@NSC-15/g-C_3N_4 shows a slightly higher specific surface area (83 m^2 g^{-1}) compared to g-C_3N_4 (76 m^2 g^{-1}) and CoZn@NC/g-C_3N_4 (80 m^2 g^{-1}), as presented in Table S1.† However, the pore size distribution curve shows that the pore size distribution and pore volume of CoZnS@NSC-15/g-C_3N_4 are rather smaller than those of g-C_3N_4 and CoZn@NC/g-C_3N_4, as displayed in Fig. S5 and Table S1.† This may be caused by the collapse of the pores in CoZn@NC during the sulfidation process. This high specific surface area and the presence of a large number of microporous structures provide a good basis for excellent photocatalytic performance.

The chemical composition and states of the as-obtained samples were measured using X-ray photoelectron spectroscopy (XPS). The XPS survey spectra of g-C_3N_4, CoZn@NC/g-C_3N_4, and CoZnS@NSC-15/g-C_3N_4 are presented in Fig. 3a. The XPS survey spectra of bare g-C_3N_4 confirm the presence of C, N, and O elements; the CoZn@NC/g-C_3N_4 composite shows the presence of C, N, O, Co, and Zn elements, while the sulfidated CoZnS@NSC-15/g-C_3N_4 nanocomposite shows the presence of C, N, O, S, Co, and Zn elements. As presented in Fig. 3b, the enlarged survey spectrum clearly demonstrates the
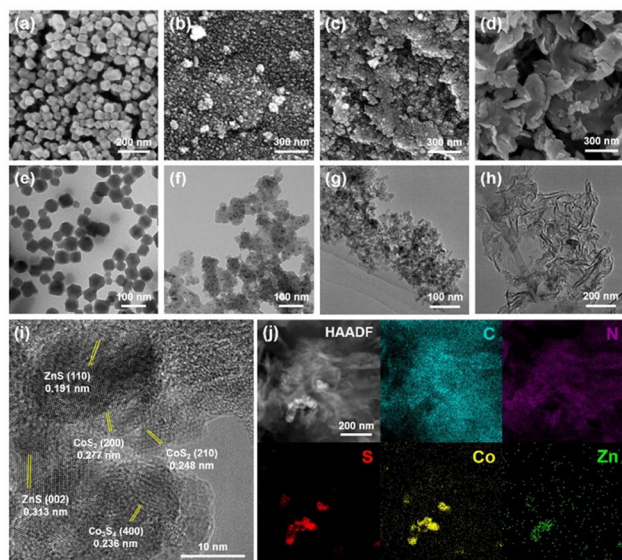

Fig. 2 (a–d) SEM and (e–h) TEM images of CoZn-MoF, CoZn@NC, CoZnS@NSC-15, and CoZnS@NSC-15/g-C_3N_4 samples. (i) HRTEM image of the CoZnS@NSC-15/g-C_3N_4 sample. (j) HAADF-STEM and its corresponding EDX elemental images of the CoZnS@NSC-15/g-C_3N_4 sample.

3438 | *Inorg. Chem. Front.*, 2024, **11**, 3435–3445
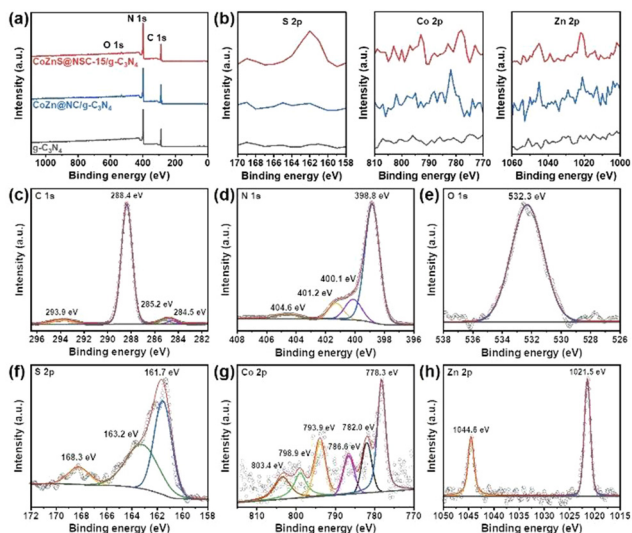
This journal is © the Partner Organisations 2024

Fig. 3 (a) XPS survey spectrum and (b) enlarged S 2p, Co 2p, and Zn 2p of g-C$_3$N$_4$, CoZn@NC/g-C$_3$N$_4$, and CoZnS@NSC-15/g-C$_3$N$_4$ samples. High-resolution XPS spectra of (c) C 1s, (d) N 1s, (e) O 1s, (f) S 2p, (g) Co 2p, and (h) Zn 2p for the CoZnS@NSC-15/g-C$_3$N$_4$ nanocomposite.

presence of the S element in the CoZnS@NSC-15/g-C$_3$N$_4$ nanocomposite, while no S element is identified in g-C$_3$N$_4$ and CoZn@NC/g-C$_3$N$_4$ samples. Similarly, the presence of Co and Zn elements can be clearly seen in CoZn@NC/g-C$_3$N$_4$ and CoZnS@NSC-15/g-C$_3$N$_4$, while no Co and Zn elements are detected in bare g-C$_3$N$_4$. The high-resolution C 1s spectra of CoZnS@NSC-15/g-C$_3$N$_4$ show four peaks at 284.5, 285.2, 288.4, and 293.9 eV (Fig. 3c), which are associated with C–C/C=C, C–N/C=N, N–C=N, and carbon satellite peaks, respectively. As depicted in Fig. 3d, the N 1s spectra of CoZnS@NSC-15/g-C$_3$N$_4$ display four peaks at 398.8, 400.1, 401.2, and 404.6 eV, which are assigned to N/C–N=C, N–(C)$_3$, N/C–N–H, and π-excitation, respectively.[50,61] As presented in Fig. 3e, the O 1s spectra are deconvoluted into one peak (532.3 eV),[62,63] which is attributed to the lattice oxygen atoms within the CoZnS@NSC-15/g-C$_3$N$_4$ system. The S 2p spectrum is deconvoluted into three peaks at 161.7, 163.2, and 168.3 eV (Fig. 3f), which are attributed to S 2p$_{3/2}$, S 2p$_{1/2}$, and satellite peaks of S 2p, respectively.[64,65] The high-resolution Co 2p spectra are divided into six peaks, as displayed in Fig. 3g. The peaks at 782.0 and 798.9 eV are associated with Co^{2+}, whereas the peaks at 778.3 and 793.9 eV are ascribed to Co^{3+}.[66] Moreover, the peaks at 786.6 and 803.4 eV are the satellite peaks of Co^{2+} and Co^{3+}, respectively.[67,68] The cobalt ions exhibit two valence states, which is consistent with the XRD detection of Co$_3$S$_4$. The Zn 2p spectra (Fig. 3h) are divided into two firm peaks at 1021.5 and 1044.6 eV, which are assigned to Zn 2p$_{3/2}$ and Zn 2p$_{1/2}$, thus indicating the presence of Zn^{2+} ions within the CoZnS@NSC-15/g-C$_3$N$_4$ system.[64,69]

The optical absorption properties of the synthesized photocatalysts were examined using ultraviolet-visible diffuse reflectance spectroscopy (UV-Vis DRS). In contrast to g-C$_3$N$_4$ and CoZn@NC/g-C$_3$N$_4$, the CoZnS@NSC-X/g-C$_3$N$_4$ sample exhibited a red shift and improved light absorption in the visible range

with increasing CoZnS@NSC sulfidation treatment time (Fig. 4a). This result proves the successful introduction of CoZnS@NSC onto the g-C$_3$N$_4$ surface, which significantly promoted visible-light absorption. The energy band gap (E_g) of g-C$_3$N$_4$ was estimated based on the UV-vis absorption spectra using the Tauc model. As presented in Fig. S6a,† the energy band gap of g-C$_3$N$_4$ is found to be 3.02 eV via extrapolation of the linear component of the $(\alpha h v)^2$ versus $(h v)$ curve. Based on the valence band (VB) XPS spectra (Fig. S6b†), the valence band energy (E_{VB}) of g-C$_3$N$_4$ is estimated to be 2.26 eV, while the conduction band energy (E_{CB}) is typically calculated by subtracting E_g from E_{VB}; thus the E_{CB} of g-C$_3$N$_4$ is found to be −0.76 eV.

To deeply understand the charge behavior, ultraviolet photoelectron spectroscopy (UPS) with a monochromatic HeI light source (21.22 eV) was employed to evaluate the band configurations of g-C$_3$N$_4$, CoZn@NC and CoZnS@NSC-15 nanoparticles. According to the equation, $\Phi = 21.22 - E_{cutoff}$,[70] the work function (Φ) of g-C$_3$N$_4$ is found to be 4.30 eV versus normalized hydrogen electrode (NHE), which is in agreement with the test results of previous studies (Fig. 4b).[71] According to previous studies, the Φ values of CoS$_2$, Co$_3$S$_4$, and ZnS are higher than that of g-C$_3$N$_4$,[72–74] which confirms the rapid migration of charge carriers from g-C$_3$N$_4$ to sulfides, which inherently steers the spatial separation of photogenerated e$^-$/h$^+$ pairs. As displayed in Fig. 4b, the Φ values of CoZn@NC and CoZnS@NSC-15 are 4.87 eV and 4.45 eV, respectively. Fig. S7† shows that the Φ values of CoZnS@NSC-30, CoZnS@NSC-45, and CoZnS@NSC-60 with longer sulfidation time are 4.42, 4.38, and 4.35 eV, respectively, which proves that the internal built-in electric-field intensity decreases at the interface between g-C$_3$N$_4$ and CoZnS@NSC with an increasing sulfidation time. This leads to a reduction in the efficiency of photoexcited charge carriers, which in turn gradually decreases the photocatalytic H$_2$ production activity with increasing sulfidation duration.

Photoluminescence (PL) tests evaluated the effectiveness of photogenerated e$^-$/h$^+$ pairs. Fig. 5a shows the PL spectra of the g-C$_3$N$_4$, CoZn@NC/g-C$_3$N$_4$, and CoZnS@NSC-15/g-C$_3$N$_4$ samples. The as-synthesized samples display a prominent peak around 435 nm. It is noteworthy that the peak intensity of CoZnS@NSC-15/g-C$_3$N$_4$ significantly reduced compared to

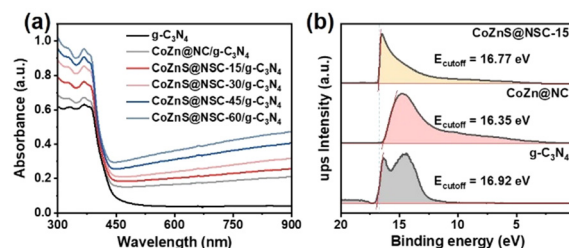**Fig. 4** (a) UV-Vis DRS spectra of the as-prepared samples. (b) Onset level of the secondary electron cutoff of the UPS spectra of g-C$_3$N$_4$, CoZn@NC, and CoZnS@NSC-15 nanoparticles.
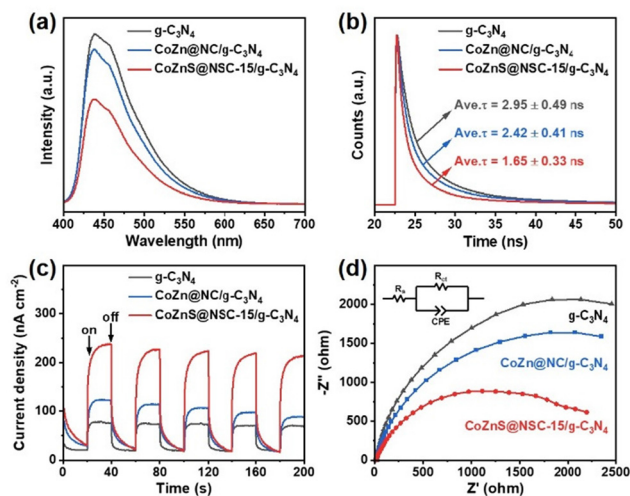
Fig. 5 (a) PL emission spectra, (b) TRPL decay spectra, (c) TPR, and (d) EIS Nyquist curves of g-C$_3$N$_4$, CoZn@NC/g-C$_3$N$_4$, and CoZnS@NSC-15/g-C$_3$N$_4$.

those of bare g-C$_3$N$_4$ and unsulfidated CoZn@NC/g-C$_3$N$_4$, suggesting that sulfidated CoZnS@NSC nanoparticles are beneficial for hindering e$^-$/h$^+$ pair recombination. Additionally, time-resolved photoluminescence (TRPL) spectra were collected to determine the lifetime of photogenerated charge carriers. Fig. 5b and Table S2† show that g-C$_3$N$_4$, CoZn@NC/g-C$_3$N$_4$, and CoZnS@NSC-15/g-C$_3$N$_4$ have excited state lifetimes of 2.95 ± 0.49 ns, 2.42 ± 0.41 ns, and 1.65 ± 0.33 ns. This decrease in lifetime indicates the rapid migration and separation efficiency of photogenerated charge carriers. This result suggests that the incorporation of CoZnS@NSC onto g-C$_3$N$_4$ is more beneficial for lowering the charge carrier lifetime to that of unsulfidated CoZn@NC, which promotes charge transfer and separation.

Furthermore, the charge carrier characteristics of g-C$_3$N$_4$, CoZn@NC/g-C$_3$N$_4$, and CoZnS@NSC-15/g-C$_3$N$_4$ photocatalysts were examined by a photocurrent test conducted in a traditional three-electrode cell with multiple on–off visible-light irradiation stages. As depicted in Fig. 5c, the transient photocurrent response (TPR) of CoZnS@NSC-15/g-C$_3$N$_4$ > CoZn@NC/g-C$_3$N$_4$ > g-C$_3$N$_4$ indicates the substantial improvements in the separation and transport of photoexcited e$^-$/h$^+$ pairs in the presence of CoZnS@NSC as compared to those of CoZn@NC nanoparticles. In addition, the electrochemical impedance spectroscopy (EIS) Nyquist measurements were carried out to assess the interfacial charge-migration resistance of the as-obtained samples. The EIS Nyquist plot obviously shows that CoZnS@NSC-15/g-C$_3$N$_4$ has a smaller angle radius than CoZn@NC/g-C$_3$N$_4$ and g-C$_3$N$_4$ (Fig. 5d), indicating that the incorporation of CoZnS@NSC significantly lowers charge migration resistance and boosts electronic conductivity. Overall, the TPR and EIS results show that the introduction of CoZnS@NSC into g-C$_3$N$_4$ promotes photogenerated e$^-$/h$^+$ pairs, leading to enhanced photocatalytic H$_2$ generation.

The photocatalytic H$_2$ production activity with visible-light illumination was measured to obtain the optimal H$_2$ production conditions and to compare the H$_2$ production rates of different samples. As presented in Fig. 6a, among the tested sacrificial agents, the suitable redox potential of triethanolamine (TEOA) and the basic environment created can significantly increase the photocatalytic hydrogen production. Additionally, the remarkable hydrophilic properties of TEOA make it more susceptible to be adsorbed on the g-C$_3$N$_4$ surface. Taken together, these aspects establish TEOA as an effective sacrificial agent for g-C$_3$N$_4$. Furthermore, a series of comparative experiments were conducted to determine the optimal weight content of CoZnS@NSC-15 (Fig. S8†). The result indicates that 10% is the optimal weight content of the CoZnS@NSC-15 cocatalyst in CoZnS@NSC-15/g-C$_3$N$_4$ nanocomposites. When the loading amount of ConZnS@NSC-15 on g-C$_3$N$_4$ is further increased, the photocatalytic activity for H$_2$ production shows a decreasing trend. Fig. 6b depicts the H$_2$ production performance of the as-prepared photocatalysts. For bare g-C$_3$N$_4$, negligible H$_2$ production occurred due to the rapid recombination of charge carriers and low visible-light adsorption. It was also found that the rate of photocatalytic H$_2$ evolution initially increases and then decreases with increasing sulfidation time. The optimal sample CoZnS@NSC-15/g-C$_3$N$_4$ exhibits the highest H$_2$ evolution rate (610.8 μmol h^{-1} g^{-1}) among all the as-prepared photocatalysts, which is almost 290.9 and 3.7-fold higher than those of bare g-C$_3$N$_4$ and CoZn@NC/g-C$_3$N$_4$, respectively. Noticeably, the photocatalytic performance of CoZnS@NSC-15/g-C$_3$N$_4$ exceeds that of previously reported co-catalyst modified g-C$_3$N$_4$-based photocatalysts (Table S3†). The results demonstrate the significance of an optimal sulfidation time of CoZnS@NSC nanoparticles in
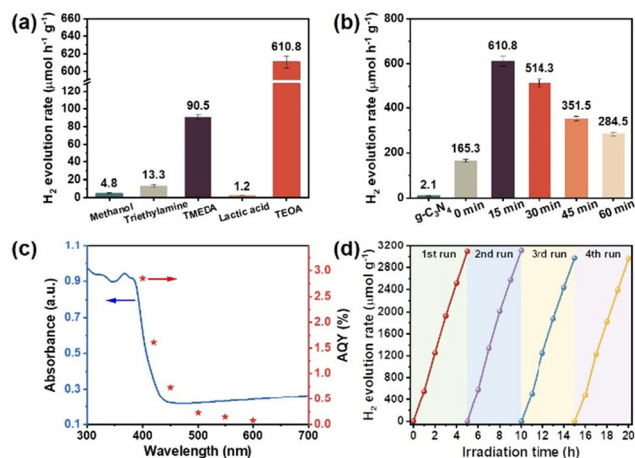
Fig. 6 (a) Photocatalytic H$_2$ evolution rates over the CoZnS@NSC-15/g-C$_3$N$_4$ composite employing various sacrificial agents. (b) H$_2$ generation rates over g-C$_3$N$_4$, CoZn@NC/g-C$_3$N$_4$ and CoZnS@NSC-X/g-C$_3$N$_4$ after sulfidation for 15, 30, 45, and 60 min. (c) Wavelength-dependent AQY values of H$_2$ evolution for the CoZnS@NSC-15/g-C$_3$N$_4$ sample. (d) Photocatalytic H$_2$ stability test of the CoZnS@NSC-15/g-C$_3$N$_4$ photocatalyst.

enhancing the photocatalytic H_2 evolution activity of CoZnS@NSC-X/g-C_3N_4.

The apparent quantum yield (AQY) of CoZnS@NSC-15/g-C_3N_4 was determined at different monochromatic light illumination wavelengths (λ = 400, 420, 450, 500, 550, and 600 ± 5 nm). As demonstrated in Fig. 6c, the maximum AQY of 2.85% was observed at a wavelength of 400 nm. It is notable that the AQY decreases with the increasing value of wavelength, which is consistent with the UV-vis absorption spectra of the ConZnS@NSC-15/g-C_3N_4 photocatalyst. The recycling experiments were performed to evaluate the stability of the CoZnS@NSC-15/g-C_3N_4 photocatalyst. Fig. 6d shows that no obvious decrease in H_2 evolution is noticed even after 4 repeated cycles in the same environment. The XRD and high-resolution XPS spectroscopy (Fig. S9 and S10†) evaluation of the CoZnS@NSC-15/g-C_3N_4 sample after the stability experiment shows no significant alteration compared to that before the stability experiment. This result suggests that the CoZnS@NSC-15/g-C_3N_4 photocatalyst preserves outstanding stability for large-scale photocatalytic H_2 generation.

The polymeric g-C_3N_4 with a suitable band gap can be promoted to excited states to generate e^-/h^+ pairs by visible-light irradiation. Nevertheless, these photogenerated charge carriers within the stimulated g-C_3N_4 quickly recombine in the absence of a co-catalyst, resulting in a poor photocatalytic H_2 evolution performance. Therefore, a possible mechanism is proposed for photocatalytic H_2 evolution over CoZnS@NSC-/g-C_3N_4 nanocomposites based on the above results and discussion, as illustrated in Fig. 7. Under visible-light irradiation, the transition of electrons occurs from the valence band (VB) of g-C_3N_4 to its conduction band (CB), while leaving holes in the VB. Then, since the Φ values of CoS_2, Co_3S_4, and ZnS NPs are higher than that of g-C_3N_4,[71–74] the electrons in the CB of g-C_3N_4 rapidly migrate to the CoZnS@NSC intermediates to produce H_2. Simultaneously, the holes in the VB of g-C_3N_4 are

consumed by the TEOA to maintain the charge carrier equilibrium. Taken together, the integration of CoZnS@NSC with g-C_3N_4 results in an efficient charge carrier migration induced by the difference in their work functions, which intrinsically facilitates the spatial separation of photoinduced e^-/h^+ pairs and thus promotes the efficiency of photocatalytic H_2 production.

3. Conclusions

In summary, bimetallic CoZn-MOF derived sulfidated CoZnS@NSC nanoparticles were effectively synthesized and then integrated with g-C_3N_4 as a highly efficient co-catalyst for photocatalytic H_2 production from water splitting under visible-light irradiation ($\lambda \geq$ 400 nm). The optimized CoZnS@NSC-15/g-C_3N_4 nanocomposite exhibits a significantly enhanced photocatalytic H_2 evolution rate (610.8 μmol h^{-1} g^{-1}), which is nearly 3.7 and 290.9-fold greater than those of CoZn@NC/g-C_3N_4 (165.3 μmol h^{-1} g^{-1}) and g-C_3N_4 (2.1 μmol h^{-1} g^{-1}), respectively. The PL, TRPL, TPR, and EIS Nyquist results demonstrated efficient separation and transport of photoexcited charge carriers. Overall, the augmented photocatalytic performance of the CoZnS@NSC-15/g-C_3N_4 heterostructure is attributed to the enhanced visible-light absorption, rapid electron migration, efficient separation of photoexcited charge carriers, and synergistic effects of the sulfidated CoZnS@NSC-15 co-catalyst and g-C_3N_4 photocatalyst. In our designed CoZnS@NSC-15/g-C_3N_4 system, g-C_3N_4 served as the key light absorption material for producing e^-/h^+ pairs, and then bimetallic CoZnS@NSC nanoparticles captured the photogenerated electrons which served as the reaction active centers for H^+ reduction and H_2 production. This study provides new insights into the synergistic effects of bimetallic MOF-derived multicomponent co-catalysts and semiconductor materials for augmenting the visible-light driven photocatalytic H_2 production from water splitting and other potential applications.

Fig. 7 Schematic charge carrier transfer mechanism of photocatalytic H_2 evolution under visible-light irradiation over CoZnS@NSC/g-C_3N_4 nanocomposites.

Author contributions

X.J.L. and I.U. contributed equally to this work. A. W. X. conceived and coordinated all stages of this research. X. J. L. and I. U. prepared, characterized the catalysts, performed all experiments, and written manuscript. J. H. L., S. C. and C. Z. Y participated in some experiments. All the authors were actively involved in development of the manuscript.

Conflicts of interest

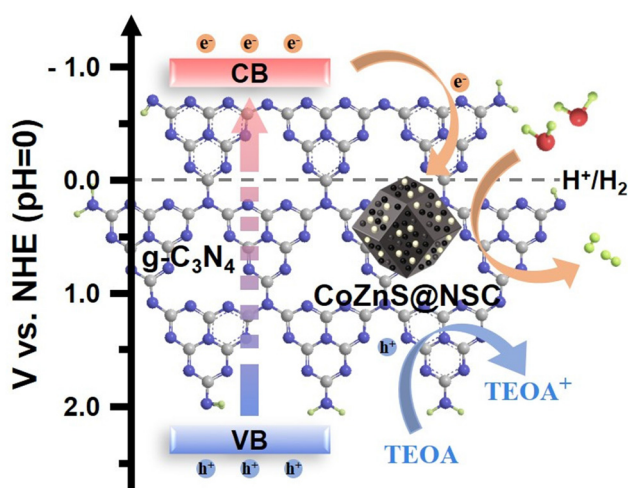The authors declare no competing financial interests.

This journal is © the Partner Organisations 2024

Inorg. Chem. Front., 2024, **11**, 3435–3445 | **3441**

Acknowledgements

References

1 C. Xia, H. Wang, J. K. Kim and J. Wang, Rational Design of Metal Oxide-Based Heterostructure for Efficient Photocatalytic and Photoelectrochemical Systems, *Adv. Funct. Mater.*, 2021, **31**, 2008247.

2 T. Liang, Y. Liu, P. Zhang, C. Liu, F. Ma, Q. Yan and Z. Dai, Interface and valence modulation on scalable phosphorene/phosphide lamellae for efficient water electrolysis, *Chem. Eng. J.*, 2020, **395**, 124976.

3 L. Cao, I. K. M. Yu, X. Xiong, D. C. W. Tsang, S. Zhang, J. H. Clark, C. Hu, Y. H. Ng, J. Shang and Y. S. Ok, Biorenewable hydrogen production through biomass gasification: A review and future prospects, *Environ. Res.*, 2020, **186**, 109547.

4 J. A. Turner, Sustainable Hydrogen Production, *Science*, 2004, **305**, 972–974.

5 H. Wang, X. Hu, Y. Ma, D. Zhu, T. Li and J. Wang, Nitrate-group-grafting-induced assembly of rutile TiO_2 nanobundles for enhanced photocatalytic hydrogen evolution, *Chin. J. Catal.*, 2020, **41**, 95–102.

6 Y.-J. Yuan, D. Chen, Z.-T. Yu and Z.-G. Zou, Cadmium sulfide-based nanomaterials for photocatalytic hydrogen production, *J. Mater. Chem. A*, 2018, **6**, 11606–11630.

7 Z. Wang, C. Li and K. Domen, Recent developments in heterogeneous photocatalysts for solar-driven overall water splitting, *Chem. Soc. Rev.*, 2019, **48**, 2109–2125.

8 S. Ma, Y. Deng, J. Xie, K. He, W. Liu, X. Chen and X. Li, Noble-metal-free Ni_3C cocatalysts decorated CdS nanosheets for high-efficiency visible-light-driven photocatalytic H_2 evolution, *Appl. Catal., B*, 2018, **227**, 218–228.

9 D. Ma, Z. Zhang, Y. Zou, J. Chen and J.-W. Shi, The progress of g-C_3N_4 in photocatalytic H_2 evolution: From fabrication to modification, *Coord. Chem. Rev.*, 2024, **500**, 215489.

10 Z. Wang, M. Murugananthan and Y. Zhang, Graphitic carbon nitride based photocatalysis for redox conversion of arsenic(III) and chromium(VI) in acid aqueous solution, *Appl. Catal., B*, 2019, **248**, 349–356.

11 Y.-N. Liu, C.-C. Shen, N. Jiang, Z.-W. Zhao, X. Zhou, S.-J. Zhao and A.-W. Xu, g-C_3N_4 Hydrogen-Bonding Viologen for Significantly Enhanced Visible-Light Photocatalytic H_2 Evolution, *ACS Catal.*, 2017, **7**, 8228–8234.

12 X.-X. Fang, L.-B. Ma, K. Liang, S.-J. Zhao, Y.-F. Jiang, C. Ling, T. Zhao, T.-Y. Cheang and A.-W. Xu, The doping of phosphorus atoms into graphitic carbon nitride for highly enhanced photocatalytic hydrogen evolution, *J. Mater. Chem. A*, 2019, **7**, 11506–11512.

13 J. Gao, Y. Wang, S. Zhou, W. Lin and Y. Kong, A Facile One-Step Synthesis of Fe-Doped g-C_3N_4 Nanosheets and Their Improved Visible-Light Photocatalytic Performance, *ChemCatChem*, 2017, **9**, 1708–1715.

14 Y.-S. Jun, E. Z. Lee, X. Wang, W. H. Hong, G. D. Stucky and A. Thomas, From Melamine-Cyanuric Acid Supramolecular Aggregates to Carbon Nitride Hollow Spheres, *Adv. Funct. Mater.*, 2013, **23**, 3661–3667.

15 Y. Xing, X. Wang, S. Hao, X. Zhang, X. Wang, W. Ma, G. Zhao and X. Xu, Recent advances in the improvement of g-C_3N_4 based photocatalytic materials, *Chin. Chem. Lett.*, 2021, **32**, 13–20.

16 I. Ullah, C. Ling, J.-H. Li, X.-J. Lu, Z. Yang, G. Wang and A.-W. Xu, Metallic TiN nanoparticles loaded on g-C_3N_4 for plasmon enhanced visible and NIR photocatalytic H_2 evolution from water splitting, *Inorg. Chem. Front.*, 2023, **10**, 3326–3334.

17 Y. Lv, D. Ma, K. Song, S. Mao, Z. Liu, D. He, X. Zhao, T. Yao and J.-W. Shi, Graphitic carbon nitride decorated with C–N compounds broken by s-triazine unit as homojunction for photocatalytic H_2 evolution, *J. Mater. Chem. A*, 2023, **11**, 800–808.

18 Y. Lv, D. Ma, C. Yang, K. Song, L. Shi, Y. Cheng, C. Niu and J.-W. Shi, *In situ* construction of lead-free halide perovskite $CsCu_2I_3$/g-C_3N_4 heterojunction for photocatalytic H_2 generation, *Sep. Purif. Technol.*, 2023, **316**, 123813.

19 B.-B. Xu, X.-B. Fu, X.-M. You, E. Zhao, F.-F. Li, Z. Chen, Y.-X. Li, X. L. Wang and Y.-F. Yao, Synergistic Promotion of Single-Atom Co Surrounding a PtCo Alloy Based On a g-C_3N_4 Nanosheet for Overall Water Splitting, *ACS Catal.*, 2022, **12**, 6958–6967.

20 J. Luo, H. Han, X. Wang, X. Qiu, B. Liu, Y. Lai, X. Chen, R. Zhong, L. Wang and C. Wang, Single-atom Nb anchored on graphitic carbon nitride for boosting electron transfer towards improved photocatalytic performance, *Appl. Catal., B*, 2023, **328**, 122495.

21 M. Kombo, H.-B. Chong, L.-B. Ma, S. Sahar, X.-X. Fang, T. Zhao, C. Ling, X.-J. Lu and A.-W. Xu, Graphitic Carbon Nitride Decorated with Nickel(II)-(3-Pyridyl) Benzimidazole Complexes and Pt Nanoparticles as a Cocatalyst for Photocatalytic Hydrogen Production from Water Splitting, *ACS Appl. Nano Mater.*, 2020, **3**, 10659–10667.

22 A. Mishra, A. Mehta, S. Basu, N. P. Shetti, K. R. Reddy and T. M. Aminabhavi, Graphitic carbon nitride (g-C_3N_4)–based metal-free photocatalysts for water splitting: A review, *Carbon*, 2019, **149**, 693–721.

23 S. Sun, X. Zhang, X. Liu, L. Pan, X. Zhang and J. Zou, Design and Construction of Cocatalysts for Photocatalytic Water Splitting, *Acta Phys.-Chim. Sin.*, 2020, **36**, 1905007.

24 C. Li, Y. Du, D. Wang, S. Yin, W. Tu, Z. Chen, M. Kraft, G. Chen and R. Xu, Unique P–Co–N Surface Bonding States Constructed on g-C_3N_4 Nanosheets for Drastically

3442 | *Inorg. Chem. Front.*, 2024, **11**, 3435–3445

This journal is © the Partner Organisations 2024

Enhanced Photocatalytic Activity of H_2 Evolution, *Adv. Funct. Mater.*, 2017, **27**, 1604328.

25 Z. Liang, B. Sun, X. Xu, H. Cui and J. Tian, Metallic 1T-phase MoS_2 quantum dots/g-C3N4 heterojunctions for enhanced photocatalytic hydrogen evolution, *Nanoscale*, 2019, **11**, 12266–12274.

26 R. Shen, J. Xie, Y. Ding, S.-y. Liu, A. Adamski, X. Chen and X. Li, Carbon Nanotube-Supported Cu_3P as High-Efficiency and Low-Cost Cocatalysts for Exceptional Semiconductor-Free Photocatalytic H_2 Evolution, *ACS Sustainable Chem. Eng.*, 2019, **7**, 3243–3250.

27 T. Chen, C. Song, M. Fan, Y. Hong, B. Hu, L. Yu and W. Shi, *In situ* fabrication of CuS/g-C3N4 nanocomposites with enhanced photocatalytic H_2-production activity via photoinduced interfacial charge transfer, *Int. J. Hydrogen Energy*, 2017, **42**, 12210–12219.

28 Y. Peng, L. Zhou, L. Wang, J. Lei, Y. Liu, S. Daniele and J. Zhang, Preparation of NiCoP-decorated g-C3N4 as an efficient photocatalyst for H_2O_2 production, *Res. Chem. Intermed.*, 2019, **45**, 5907–5917.

29 Q. Ji, L. Pan, J. Xu, C. Wang and L. Wang, Zeolitic Imidazolate Framework-67-Derived CoP/Co@N,P-Doped Carbon Nanoparticle Composites with Graphitic Carbon Nitride for Enhanced Photocatalytic Production of H_2 and H_2O_2, *ACS Appl. Nano Mater.*, 2020, **3**, 3558–3567.

30 A. Irshad and N. Munichandraiah, Electrodeposited Nickel–Cobalt–Sulfide Catalyst for the Hydrogen Evolution Reaction, *ACS Appl. Mater. Interfaces*, 2017, **9**, 19746–19755.

31 X. Gao, J. Wang, D. Zhang, K. Adair, K. Feng, N. Sun, H. Zheng, H. Shao, J. Zhong, Y. Ma, X. Sun and X. Sun, Carbon coated bimetallic sulfide nanodots/carbon nanorod heterostructure enabling long-life lithium-ion batteries, *J. Mater. Chem. A*, 2017, **5**, 25625–25631.

32 H.-W. Man, C.-S. Tsang, M. M.-J. Li, J. Mo, B. Huang, L. Y. S. Lee, Y.-c. Leung, K.-Y. Wong and S. C. E. Tsang, Transition metal-doped nickel phosphide nanoparticles as electro- and photocatalysts for hydrogen generation reactions, *Appl. Catal., B*, 2019, **242**, 186–193.

33 K. Wu, Z. Chen, W.-C. Cheong, S. Liu, W. Zhu, X. Cao, K. Sun, Y. Lin, L. Zheng, W. Yan, Y. Pan, D. Wang, Q. Peng, C. Chen and Y. Li, Toward Bifunctional Overall Water Splitting Electrocatalyst: General Preparation of Transition Metal Phosphide Nanoparticles Decorated N-Doped Porous Carbon Spheres, *ACS Appl. Mater. Interfaces*, 2018, **10**, 44201–44208.

34 L. Kong, M. Zhong, W. Shuang, Y. Xu and X.-H. Bu, Electrochemically active sites inside crystalline porous materials for energy storage and conversion, *Chem. Soc. Rev.*, 2020, **49**, 2378–2407.

35 L. Cheng, Q. Zhang, M. Xu, Q. Zhai and C. Zhang, Two-for-one strategy: Three-dimensional porous Fe-doped Co_3O_4 cathode and N-doped carbon anode derived from a single bimetallic metal-organic framework for enhanced hybrid supercapacitor, *J. Colloid Interface Sci.*, 2021, **583**, 299–309.

36 X. Ge, H. Di, P. Wang, X. Miao, P. Zhang, H. Wang, J. Ma and L. Yin, Metal–Organic Framework-Derived Nitrogen-Doped Cobalt Nanocluster Inlaid Porous Carbon as High-Efficiency Catalyst for Advanced Potassium–Sulfur Batteries, *ACS Nano*, 2020, **14**, 16022–16035.

37 M. Ding, R. W. Flaig, H.-L. Jiang and O. M. Yaghi, Carbon capture and conversion using metal–organic frameworks and MOF-based materials, *Chem. Soc. Rev.*, 2019, **48**, 2783–2828.

38 W. Zhou, D.-D. Huang, Y.-P. Wu, J. Zhao, T. Wu, J. Zhang, D.-S. Li, C. Sun, P. Feng and X. Bu, Stable Hierarchical Bimetal–Organic Nanostructures as High Performance Electrocatalysts for the Oxygen Evolution Reaction, *Angew. Chem., Int. Ed.*, 2019, **58**, 4227–4231.

39 B. Chen, D. Kim, Z. Zhang, M. Lee and K. Yong, MOF-derived NiCoZnP nanoclusters anchored on hierarchical N-doped carbon nanosheets array as bifunctional electrocatalysts for overall water splitting, *Chem. Eng. J.*, 2021, **422**, 130533.

40 Q. Wang and D. Astruc, State of the Art and Prospects in Metal–Organic Framework (MOF)-Based and MOF-Derived Nanocatalysis, *Chem. Rev.*, 2020, **120**, 1438–1511.

41 Z. Chen, H. Qing, K. Zhou, D. Sun and R. Wu, Metal-organic framework-derived nanocomposites for electrocatalytic hydrogen evolution reaction, *Prog. Mater. Sci.*, 2020, **108**, 100618.

42 J. Zhao, X. Zhang, M. Liu, Y.-Z. Jiang, M. Wang, Z.-Y. Li and Z. Zhou, Metal–organic-framework-derived porous 3D heterogeneous $NiFe_x$/$NiFe_2O_4$@NC nanoflowers as highly stable and efficient electrocatalysts for the oxygen-evolution reaction, *J. Mater. Chem. A*, 2019, **7**, 21338–21348.

43 Z. Chen, R. Wu, H. Wang, Y. Jiang, L. Jin, Y. Guo, Y. Song, F. Fang and D. Sun, Construction of hybrid hollow architectures by *in situ* rooting ultrafine ZnS nanorods within porous carbon polyhedra for enhanced lithium storage properties, *Chem. Eng. J.*, 2017, **326**, 680–690.

44 X. Sun, H. Huang, C. Wang, Y. Liu, T.-L. Hu and X.-H. Bu, Effective Co_xS_y HER Electrocatalysts Fabricated by *In situ* Sulfuration of a Metal-Organic Framework, *ChemElectroChem*, 2018, **5**, 3639–3644.

45 L. Chai, Z. Hu, X. Wang, Y. Xu, L. Zhang, T.-T. Li, Y. Hu, J. Qian and S. Huang, Stringing Bimetallic Metal–Organic Framework-Derived Cobalt Phosphide Composite for High-Efficiency Overall Water Splitting, *Adv. Sci.*, 2020, **7**, 1903195.

46 J. Shi, F. Qiu, W. Yuan, M. Guo and Z.-H. Lu, Nitrogen-doped carbon-decorated yolk-shell CoP@FeCoP micro-polyhedra derived from MOF for efficient overall water splitting, *Chem. Eng. J.*, 2021, **403**, 126312.

47 H. Yu, R. Shi, Y. Zhao, G. I. N. Waterhouse, L.-Z. Wu, C.-H. Tung and T. Zhang, Smart Utilization of Carbon Dots in Semiconductor Photocatalysis, *Adv. Mater.*, 2016, **28**, 9454–9477.

48 J.-P. Zou, L.-C. Wang, J. Luo, Y.-C. Nie, Q.-J. Xing, X.-B. Luo, H.-M. Du, S.-L. Luo and S. L. Suib, Synthesis and efficient visible light photocatalytic H_2 evolution of a metal-free g-C3N4/graphene quantum dots hybrid photocatalyst, *Appl. Catal., B*, 2016, **193**, 103–109.

This journal is © the Partner Organisations 2024

Inorg. Chem. Front., 2024, **11**, 3435–3445 | **3443**

49 H. Che, G. Che, P. Zhou, C. Liu, H. Dong, C. Li, N. Song and C. Li, Nitrogen doped carbon ribbons modified g-C$_3$N$_4$ for markedly enhanced photocatalytic H$_2$-production in visible to near-infrared region, *Chem. Eng. J.*, 2020, **382**, 122870.

50 Y. Pan, K. Sun, S. Liu, X. Cao, K. Wu, W.-C. Cheong, Z. Chen, Y. Wang, Y. Li, Y. Liu, D. Wang, Q. Peng, C. Chen and Y. Li, Core–Shell ZIF-8@ZIF-67-Derived CoP Nanoparticle-Embedded N-Doped Carbon Nanotube Hollow Polyhedron for Efficient Overall Water Splitting, *J. Am. Chem. Soc.*, 2018, **140**, 2610–2618.

51 J. Chang, Y. Wang, L. Chen, D. Wu, F. Xu, Z. Bai, K. Jiang and Z. Gao, Cobalt nanoparticles embedded nitrogen doped carbon, preparation from alkali deprotonation assisted ZIF-67 and its electrocatalytic performance in oxygen evolution reaction, *Int. J. Hydrogen Energy*, 2020, **45**, 12787–12797.

52 H. Li, Y. Su, W. Sun and Y. Wang, Carbon Nanotubes Rooted in Porous Ternary Metal Sulfide@N/S-Doped Carbon Dodecahedron: Bimetal-Organic-Frameworks Derivation and Electrochemical Application for High-Capacity and Long-Life Lithium-Ion Batteries, *Adv. Funct. Mater.*, 2016, **26**, 8345–8353.

53 W. Sun, J. Zhu and Y. Zheng, Graphitic carbon nitride heterojunction photocatalysts for solar hydrogen production, *Int. J. Hydrogen Energy*, 2021, **46**, 37242–37267.

54 J. Yan, Y. Huang, C. Chen, X. Liu and H. Liu, The 3D CoNi alloy particles embedded in N-doped porous carbon foams for high-performance microwave absorbers, *Carbon*, 2019, **152**, 545–555.

55 Q. Jin, W. Li, K. Wang, P. Feng, H. Li, T. Gu, M. Zhou, W. Wang, S. Cheng and K. Jiang, Experimental design and theoretical calculation for sulfur-doped carbon nanofibers as a high performance sodium-ion battery anode, *J. Mater. Chem. A*, 2019, **7**, 10239–10245.

56 X. Sun, C. Wang, Y. Gong, L. Gu, Q. Chen and Y. Yu, A Flexible Sulfur-Enriched Nitrogen Doped Multichannel Hollow Carbon Nanofibers Film for High Performance Sodium Storage, *Small*, 2018, **14**, 1802218.

57 Z. Hong, Y. Zhen, Y. Ruan, M. Kang, K. Zhou, J.-M. Zhang, Z. Huang and M. Wei, Rational Design and General Synthesis of S-Doped Hard Carbon with Tunable Doping Sites toward Excellent Na-Ion Storage Performance, *Adv. Mater.*, 2018, **30**, 1802035.

58 Y. Li, S. Zhu, X. Kong, Y. Liang, Z. Li, S. Wu, C. Chang, S. Luo and Z. Cui, ZIF-67 derived Co@NC/g-C$_3$N$_4$ as a photocatalyst for enhanced water splitting H$_2$ evolution, *Environ. Res.*, 2021, **197**, 111002.

59 J. Zhao, S. Hou, Y. Bai, Y. Lian, Q. Zhou, C. Ban, Z. Wang and H. Zhang, Multilayer dodecahedrons Zn-Co sulfide for supercapacitors, *Electrochim. Acta*, 2020, **354**, 136714.

60 Z. Zhang, Y. Huang, X. Liu, C. Chen, Z. Xu and P. Liu, Zeolitic imidazolate frameworks derived ZnS/Co$_3$S$_4$ composite nanoparticles doping on polyhedral carbon framework for efficient lithium/sodium storage anode materials, *Carbon*, 2020, **157**, 244–254.

61 H. Tang, R. Wang, C. Zhao, Z. Chen, X. Yang, D. Bukhvalov, Z. Lin and Q. Liu, Oxamide-modified g-C$_3$N$_4$ nanostructures: Tailoring surface topography for high-performance visible light photocatalysis, *Chem. Eng. J.*, 2019, **374**, 1064–1075.

62 L. Zhang, Z.-J. Zhao and J. Gong, Nanostructured Materials for Heterogeneous Electrocatalytic CO$_2$ Reduction and their Related Reaction Mechanisms, *Angew. Chem., Int. Ed.*, 2017, **56**, 11326–11353.

63 L. Shen, H. Lv, S. Chen, P. Kopold, P. A. van Aken, X. Wu, J. Maier and Y. Yu, Peapod-like Li$_3$VO$_4$/N-Doped Carbon Nanowires with Pseudocapacitive Properties as Advanced Materials for High-Energy Lithium-Ion Capacitors, *Adv. Mater.*, 2017, **29**, 1700142.

64 H. Tong, W. Bai, S. Yue, Z. Gao, L. Lu, L. Shen, S. Dong, J. Zhu, J. He and X. Zhang, Zinc cobalt sulfide nanosheets grown on nitrogen-doped graphene/carbon nanotube film as a high-performance electrode for supercapacitors, *J. Mater. Chem. A*, 2016, **4**, 11256–11263.

65 X. Yang, C. Cai, Y. Zou, C. Xiang, H. Chu, E. Yan, S. Qiu, L. Sun, F. Xu and X. Hu, Co$_3$O$_4$-doped two-dimensional carbon nanosheet as an electrode material for high-performance asymmetric supercapacitors, *Electrochim. Acta*, 2020, **335**, 135611.

66 Y. Liu, G. Jiang, S. Sun, B. Xu, J. Zhou, Y. Zhang and J. Yao, Growth of NiCo$_2$S$_4$ nanotubes on carbon nanofibers for high performance flexible supercapacitors, *J. Electroanal. Chem.*, 2017, **804**, 212–219.

67 Y. Zou, C. Cai, C. Xiang, P. Huang, H. Chu, Z. She, F. Xu, L. Sun and H.-B. Kraatz, Simple synthesis of core-shell structure of Co–Co$_3$O$_4$ @ carbon-nanotube-incorporated nitrogen-doped carbon for high-performance supercapacitor, *Electrochim. Acta*, 2018, **261**, 537–547.

68 H. Chen, M. Q. Wang, Y. Yu, H. Liu, S.-Y. Lu, S.-J. Bao and M. Xu, Assembling Hollow Cobalt Sulfide Nanocages Array on Graphene-like Manganese Dioxide Nanosheets for Superior Electrochemical Capacitors, *ACS Appl. Mater. Interfaces*, 2017, **9**, 35040–35047.

69 L. Shen, J. Wang, G. Xu, H. Li, H. Dou and X. Zhang, NiCo$_2$S$_4$ Nanosheets Grown on Nitrogen-Doped Carbon Foams as an Advanced Electrode for Supercapacitors, *Adv. Energy Mater.*, 2015, **5**, 1400977.

70 F. Shi, Z. Geng, K. Huang, Q. Liang, Y. Zhang, Y. Sun, J. Cao and S. Feng, Cobalt Nanoparticles/Black Phosphorus Nanosheets: An Efficient Catalyst for Electrochemical Oxygen Evolution, *Adv. Sci.*, 2018, **5**, 1800575.

71 Q. Liu, C. Zeng, Z. Xie, L. Ai, Y. Liu, Q. Zhou, J. Jiang, H. Sun and S. Wang, Cobalt@nitrogen-doped bamboo-structured carbon nanotube to boost photocatalytic hydrogen evolution on carbon nitride, *Appl. Catal., B*, 2019, **254**, 443–451.

72 Y. Xu and M. A. A. Schoonen, The absolute energy positions of conduction and valence bands of selected semiconducting minerals, *Am. Mineral.*, 2000, **85**, 543–556.

3444 | *Inorg. Chem. Front.*, 2024, **11**, 3435–3445

This journal is © the Partner Organisations 2024

73 R. Karimi, F. Yousefi, M. Ghaedi, K. Dashtian and G. Yasin, Unveiling charge dynamics of Co_3S_4 nanowalls/CdS nanospheres n-n heterojunction for efficient photoelectrochemical Cr(VI) detoxification and N_2 fixation, *J. Environ. Chem. Eng.*, 2022, **10**, 108549.

74 L. Pei, J. Zhong, T. Li, W. Bai, S. Wu, Y. Yuan, Y. Chen, Z. Yu, S. Yan and Z. Zou, CoS_2@N-doped carbon core–shell nanorod array grown on Ni foam for enhanced electrocatalytic water oxidation, *J. Mater. Chem. A*, 2020, **8**, 6795–6803.

This journal is © the Partner Organisations 2024

Inorg. Chem. Front., 2024, **11**, 3435–3445 | **3445**